Radiation Model of a TiO_2-Coated, Quartz Wool, Packed-Bed Photocatalytic Reactor

G. E. Imoberdorf
INTEC, Instituto de Desarrollo Tecnológico para la Industria Química (Universidad Nacional del Litoral and CONICET), Ruta Nacional No. 168, km 0, Paraje El Pozo, S3000GLM Santa Fe, Argentina

G. Vella, A. Sclafani, and L. Rizzuti
Università di Palermo, Dipartimento di Ingegneria Chimica dei Processi e dei Materiali, Unità di Ricerca INCA Palermo 2, Viale delle Scienze, Ed.6, 90128 Palermo, Italy

O. M. Alfano and A. E. Cassano
INTEC, Instituto de Desarrollo Tecnológico para la Industria Química (Universidad Nacional del Litoral and CONICET), Ruta Nacional No. 168, km 0, Paraje El Pozo, S3000GLM Santa Fe, Argentina

DOI 10.1002/aic.11863
Published online December 10, 2009 in Wiley InterScience (www.interscience.wiley.com).

The radiation field of a packed-bed photocatalytic reactor filled with quartz wool coated with titanium dioxide was modeled using the Monte Carlo technique and the following information: the radiation flux emitted by the lamps, the diameter size distribution of the quartz fiber cloth, the mass of quartz fibers and of TiO_2 that was immobilized on the fiber surface as well as the refractive index, and the spectral absorption coefficient of the materials of the system. Modeling predictions were validated with radiometer measurements of the transmitted radiation through the reactor, the root mean square error being <9.7%. Finally, by means of a parametric study, the validated model was used to analyze the effect of the design variables, such as the radii of the quartz fibers, thickness of the TiO_2 coatings, and amount of TiO_2-coated quartz wool, on the distribution and nonuniformity of the radiative energy distribution inside the reactor. © 2009 American Institute of Chemical Engineers *AIChE J,* 56: 1030–1044, 2010
Keywords: packed-bed reactor, photocatalysis, radiation modeling, quartz wool, Monte Carlo

Introduction

Photocatalytic reactors have became a subject of increasing interest because of their potential applications in pollution abatement. Many different reactor geometries and configurations have been proposed. Photocatalytic reactors utilized for the treatment of water pollutants can be classified according to whether the photocatalyst is immobilized, such as the different forms of fixed bed reactors, or the photocatalyst is in suspension in the aqueous media, such as the slurry reactors. Besides, those photocatalytic reactors in which the TiO_2 is immobilized on the surface of an inert support may likewise be divided in four principal types: (i) membrane, monoliths, or equivalent forms of catalytic wall reactors, (ii) optical fiber reactors, (iii) fluidized bed reactors, and (iv) packed bed reactors. In all cases, the knowledge of the radiation field existing in every reaction space is indispensable for a complete characterization of the reaction kinetics or for reactor design.

Among the mentioned reactors, packed-bed photocatalytic reactors offer mainly five important advantages: (1) no separation processes to remove the catalyst from the treated stream are needed, such as the ones required for slurry

Correspondence concerning this article should be addressed to O. M. Alfano at alfano@intec.unl.edu.ar

reactors; (2) it is possible to significantly increase the photocatalytic surface by using the proper filling; (3) thin films of TiO_2 can be immobilized on UV-transparent substrates and used as the reactor filling, which benefit the radiation distribution inside of the reactor; (4) the fluid dynamics of the reactor improve with respect to those reactors without filling, enhancing the mixing of reactants, which tend to reduce the undesirable diffusive resistances; and finally, (5) the packed bed reactors have less catalysts attrition problems, such as the ones present in fluidized bed reactors.

The use of packed-bed photocatalytic reactors was first proposed by Al-Ekabi and Serpone in 1988.[1] The authors analyzed the photocatalytic degradation kinetics of chlorinated phenols using three packed-bed laboratory reactors, where titanium dioxide supported on the internal surface of a glass coil and on the external surface of glass beads was used. Complete degradation was achieved when the reactors were operated in a continuous recirculation mode. Afterward, Sclafani et al.[2] studied the existence of mass transfer limitation problems in a packed-bed reactor made of spheres of pure titania, concluding that diffusive limitations are of primary importance for photocatalytic packed-bed reactors aimed to treat aqueous streams. This result suggests the need for considering and reducing possible diffusive resistances in photocatalytic reactors. Crittenden et al.[3] proposed a sequential process for groundwater treatment that starts with the pollutant adsorption in a continuous packed bed column (nonphotocatalytic) filled with an adsorbent coated with TiO_2. This process operates under cyclic mode as follows: the continuous operation of the column is stopped when the adsorbent is saturated, and it is restarted after the adsorbent is regenerated. The regeneration is conducted by washing the adsorbent with pure water while it is exposed to solar radiation to activate the photocatalyst and partially destroy the adsorbed pollutants. Simultaneously, the remaining pollutant contained in the washing stream generated by the regeneration step is eliminated in a packed-bed photocatalytic reactor filled with silica gel coated with TiO_2. Wang et al.[4] developed a packed-bed annular reactor filled with nonwoven fiber textile coated with TiO_2. This photocatalytic reactor was used to eliminate benzene contained in air. This reactor showed a good initial performance, but after 5 h of continuum operation, the reaction rate decreased by 50% due to the deactivation of the catalyst. The authors proposed an efficient method for the catalyst reactivation, which consisted in circulating air with ozone through the photocatalyst bed. Zou et al.[5] studied a packed-bed photocatalytic reactor filled with agglomerates of nanosized particles made of a mixture of TiO_2 and SiO_2. The authors concluded that the use of this composite photocatalyst enhances the efficiency of the reactor because of the combined effect of adsorption on SiO_2 and photocatalytic regeneration on TiO_2, which makes it possible to achieve a continuous treatment operation for long periods. Finally, Ibhadon et al.[6] studied the kinetics of the photocatalytic degradation of volatile organic compounds from gas phase using a TiO_2 foam packed reactor. The reactor was operated with benzene, toluene, and xylene as model pollutants, and the conversion obtained was as high as 95%. The previously described contributions were focused on reactor efficiency analysis, kinetic studies, or new photocatalyst developments, but no radiation models were proposed.

In spite of the proved high efficiency of packed-bed photocatalytic reactors for air and water treatment, there are only a few models to describe the radiation field in such reactors. Besides, it would not be possible to develop a generalized radiation model valid to every packed bed reactor, because the type, the shape, the size, and the nature of the filling will profoundly affect the relative relevance of the physical effects involved, the validity of the model assumptions, and the final selection of the most suitable approach to solve the problem. In this sense, there are remarkable differences among the available radiation models, depending on the particularities of each application. Changrani and Raupp[7,8] developed a rigorous, two-dimensional, heterogeneous model for a reticulated-foam photocatalytic reactor. The model considers the random travel of photons in cylindrical channels randomly distributed in the reactor, which simulates the reticulated-foam filling. Its numerical solution was obtained using the Monte Carlo (MC) approach. Vorontsov et al.[9] compared the efficiency of multiple fixed-bed photocatalytic reactors (using powdered, granular, and film titania beds) with the efficiency of a vibro-fluidized-bed photocatalytic reactor. The authors proposed a pseudo-homogeneous radiation model based on geometrical considerations. Alexiadis et al.[10] modeled a packed-bed reactor, using Rashing rings made of quartz, which is transparent to UV, coated with titanium dioxide. The radiative transfer equation (RTE) was numerically solved using the MC method, and considering the reactor filling as a pseudo-homogeneous medium. Loddo et al.[11] modeled the radiation absorption in an annular, packed-bed photocatalytic reactor. The model was solved applying the MC method, taking into account the complex reflection/refraction/absorption interactions between UV-radiation and the TiO_2-coated spheres that constituted the packed bed of the reactor. To the best of our knowledge, no radiation models for packed-bed photocatalytic reactors filled with TiO_2-coated quartz wool have been published in the open literature.

From the numerical methods available to solve the RTE in photocatalytic reactors, such as the Discrete Ordinate (DO) method and the MC method, the last one is generally preferred when complex geometries and configurations are involved. This mathematical approach has already been used in photocatalytic systems proving to be an effective method to tackle problems otherwise very complex. The first work on the modeling of heterogeneous photoreactors using the MC approach was presented by Spadoni et al.[12] as far back as 1978, asserting the first rigorous numerical approach for a photosensitized reaction in an annular reactor. Besides this pioneering publication and the ones previously mentioned, we can highlight the following papers, where the MC approach was successfully applied. Yokota et al.[13] proposed a pseudo-homogeneous model aimed at evaluating the propagation of radiation in a liquid system with small particles in suspension; Pasquali et al.,[14] Yokota et al.,[15] and Yang et al.[16] modeled the radiation field in slurry photocatalytic reactors considering the absorption and scattering of TiO_2; Imoberdorf et al.[17] studied the interaction between UV radiation and TiO_2-coated spheres; Brucato et al.[18] used MC simulations to validate a simplified approach (namely the Six Flux model), to numerically solve the RTE, and to improve the uniformity of radiation distribution in photoreactors[19]; and

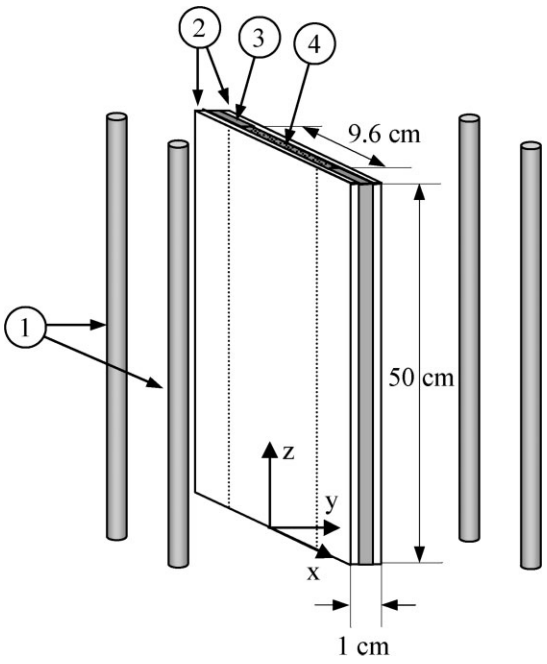

Figure 1. Geometry of the photocatalytic reactor.

(1) UV lamps, (2) borosilicate windows, (3) aluminum rod with rubber seal gaskets; (4) TiO_2-coated quartz wool.

finally, Alexiadis[20] and Singh et al.[21] analyzed the radiation distribution in photocatalytic monolith reactors.

This work deals with the radiation field predictions for a planar, packed-bed reactor made of quartz wool, coated with titanium dioxide, which is aimed to the abatement of aqueous pollutants. The numerical solution was obtained resorting to the MC method, where the following events where considered: the radiation reflection and refraction on/in the reactor windows, the photon absorption in the TiO_2 coatings, and the interaction with the quartz fibers. Modeling predictions were compared with experimental results to validate the model. Finally, the model was used to analyze the effect of TiO_2 loading, quartz wool loading, and quartz fiber radius on the radiation absorption distribution.

Experimental

Experimental setup

A packed-bed photocatalytic reactor was designed and built, in which quartz wool coated with titanium dioxide was used as photocatalyst. To minimize the inevitable radiation flux gradients inside the reactor volume, a flat geometry with a very small thickness was selected, and the reactor was irradiated from both sides with tubular lamps (Figure 1). The dimensions and the geometry of the reactor (Table 1) were defined based on the results obtained by Brucato el al.[19]

The reaction chamber was confined between two rectangular windows made of borosilicate glass, which is transparent in the useful wavelength range of UV radiation used in this work. The reactor is vertically mounted and irradiated on both sides by two UV-fluorescent lamps (Philips BL TL-K 40W/10-R) on each side. The lamps were arranged in a way

Table 1. Reactor Dimensions and Characteristics

Description	Values
Lamp	$Z_{lamp} = 60$ cm; $R_{lamp} = 1.3$ cm; $P_{eff} = 3.25$ W (output)
Reactor width	$X_{reactor} = 9.6$ cm
Reactor thickness	$Y_{reactor} = 0.5$ cm
Reactor height	$Z_{reactor} = 50$ cm
Windows	Borosilicate glass; thickness 0.25 cm
Filling	17.2 g quartz wool; 14.4% w/w of TiO_2

that allows the regulation of the distance of its axis from the reactor windows to change the radiation flux reaching the reactor. As can be noticed from Figure 1, no external reflectors were used. The lamps have an emission spectrum ranging from 340 to 420 nm, with a peak at 370 nm (Figure 2a). A quartz wool cloth, whose fibers where previously coated with a thin film of TiO_2, was placed between the reactor windows, filling completely the reaction chamber. This configuration guarantees a good contact between the aqueous pollutants and the TiO_2 catalyst surface. The reactor top and bottom heads were made of polymethylmetacrilate, with some small holes that allow the water stream to circulate.

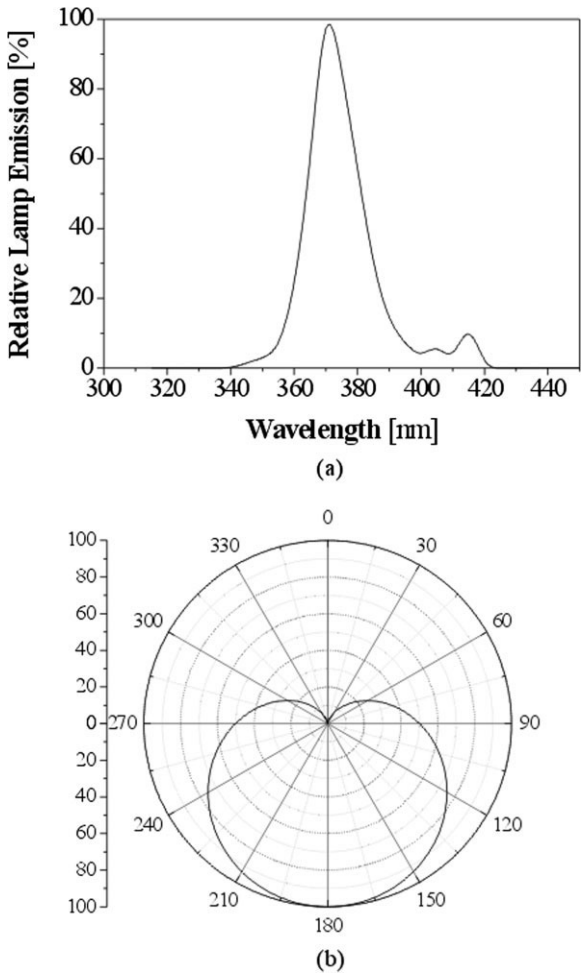

Figure 2. (a) Spectral emission of the UV lamps; (b) directional description of the lamp emission (arbitrary units).

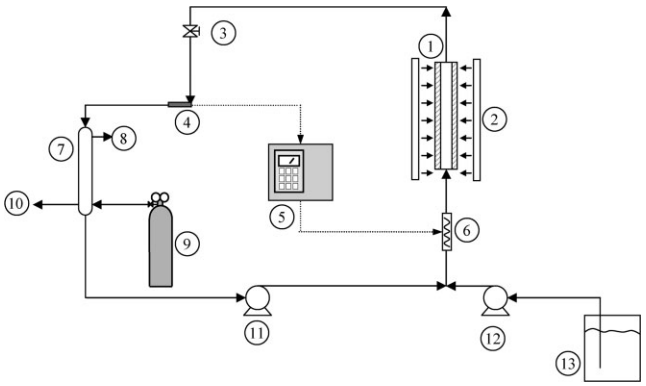

Figure 3. Flow sheet of the experimental device.

(1) Photocatalytic reactor, (2) UV lamps, (3) sample valve, (4) thermocouple, (5) PID temperature controller, (6) resistor, (7) packed column, (8) gas outlet, (9) O_2 cylinder, (10) liquid outlet, (11) recycle pump, (12) feed pump, (13) feed tank.

The aqueous stream is fed at the bottom of the reactor, passing first through the bottom head, then through the TiO_2-coated quartz wool, and finally leaves the reactor passing through the top head.

The photocatalytic reactor was coupled with complementary equipments that permit recycling the aqueous stream in a closed circuit. Figure 3 shows a schematic representation of the complete experimental setup. The recycling system comprised the photocatalytic reactor, a heat exchanger, a peristaltic pump, a fixed column where pure O_2 was injected, and the connecting tubing. The use of the recycle loop permits to operate the reactor in a differential mode. On the other hand, the use of a high flow rate in the recycle may facilitate minimization of mass transfer resistances.

Catalyst preparation

The titanium dioxide photocatalyst that was immobilized on the quartz wool (Figures 4a,b) was prepared by means of a sol–gel technique. A first solution was prepared by mixing 20 ml of Ti(IV) isopropoxide with 500 ml of isopropyl alcohol, and then an additional amount (520 ml) of isopropyl alcohol was added. This solution was mixed during 15 min. A second solution was prepared by adding 91 ml of isopropyl alcohol to 65 ml of 0.1 N solution of bidistilled water and HCl at pH = 1. These two solutions were mixed together to obtain a whitish sol with small TiO_2 particles. On the other hand, 17.2 g of quartz wool were treated for 3 h with a pH = 3 HCl solution and then dried in an oven at 55°C for 12 h. The quartz wool was soaked in the TiO_2 sol to become impregnated with the catalyst. Afterward, the cloth was drained and dried in an oven at 55°C during 12 h to remove the water and the residual isopropyl alcohol. Then, it was maintained in the oven at 250°C for 3 h to remove the chlorinated substances formed during the treatment. To increase the adherence of the TiO_2 film to the quartz fibers, the soaking and the successive steps in the oven were repeated four times. To induce the formation of TiO_2 in the anatase crystalline form, the coated quartz wool was maintained in an annealing furnace at 400°C during 4 h.

After the TiO_2 immobilization procedure was completed, the cloth was washed several times with bidistilled water. A sample of the water of the last washing was analyzed to verify that all the chlorine ions were effectively removed from the catalyst, as these ions could negatively affect the photo assisted process, and also to verify the possible presence of nonvolatile organic compounds. The absence of chlorine ions in the sample of the washing water was confirmed after adding 0.1 N $AgNO_3$ solution and observing that no precipitate was formed. Meanwhile, the absence of organic carbon was confirmed by using a total organic carbon (TOC) analyzer.

The quartz wool was accommodated inside the reactor, and other washings were performed to remove the unsuccessfully fixed excess of TiO_2. After each washing, the water samples were analyzed by means of a SHIMADZU UV-2401 PC spectrophotometer to measure the TiO_2 concentration. The quartz wool was washed several times, until no TiO_2 was detected in the washing water.

Finally, the amount of TiO_2 fixed over the quartz wool was determined by using flame atomic absorption spectroscopy (FAAS, C_2H_2/N_2O) and inductively coupled plasma optical emission spectroscopy (ICP-OES). The obtained mean value was 144 mg of TiO_2 per gram of bed. The TiO_2 catalyst is then 14.4% w/w of the entire bed mass (quartz wool + TiO_2). From XRD measurements, it was concluded that all the immobilized TiO_2 was in the anatase crystalline form.

Radiation field measurements

Measurements of the radiation flux that reaches the reactor and that is transmitted through the reactor were performed using a research radiometer (UVX Digital). The sensor used (UVX-36 sensor) has a band-pass range from 300 to 400 nm, with a maximum response at 360 nm. The measurements were made as follows. On one hand, after removing the reactor and turning on the two lamps placed at one side of the position destined to the reactor, the sensor of the radiometer was located at different positions corresponding to the receiving reactor window; in this way, the radiative flux reaching the reactor windows was measured. This procedure was repeated after placing the lamps at four different distances from the reactor. On the other hand, a second set of measurement was made after setting the reactor packed with the TiO_2-coated quartz wool in its corresponding location, and placing the sensor of the radiometer at different positions on the reactor window opposite the lamps. The radiation flux measured in this way corresponds to the transmitted radiation through the reactor. These experiments were made at several points on the reactor surfaces and different prescribed distances of the lamp axes to the mentioned windows.

Model Development

Definitions

The local net spectral radiation flux is defined as follows:

$$q_\lambda(\mathbf{x}) = \int_\Omega I_\lambda\,(\mathbf{x},\Omega)\Omega\cdot\mathbf{n}\,d\Omega = \int_{\theta_0=0}^{\pi/2}\int_{\phi_0=0}^{2\pi} \times I_\lambda(x_p, y_p, z_p, \phi_0, \theta_0)\sin\,\theta_0\,\cos\,\theta_0\,d\phi_0\,d\theta_0, \quad (1)$$

where $I_\lambda(\mathbf{x},\Omega)$ is the spectral radiation intensity associated with the energy of the beam reaching a given surface, defined by its outwardly directed unit normal vector **n**, located at point **x**, with a direction of propagation $\Omega = \Omega(\theta_0, \phi_0, 1)$ and $d\Omega = \sin\theta_0 d\phi_0 d\theta_0$ is the differential solid angle around the direction of propagation Ω.

The local net radiation flux considers the complete wavelength range of the radiation reaching the surface as follows:

$$q(\mathbf{x}) = \int_{\lambda_{\min}}^{\lambda_{\max}} q_\lambda(\mathbf{x}) d\lambda = \sum_{\lambda_{\min}}^{\lambda_{\max}} q_\lambda(\mathbf{x}). \tag{2}$$

The spectral incident radiation is given as follows:

$$G_\lambda(\mathbf{x}) = \int_{\Omega} I_\lambda(\mathbf{x},\Omega) d\Omega = \int_{\theta=0}^{\pi} \int_{\phi=0}^{2\pi} I_\lambda(x,y,z,\phi,\theta) \sin\theta \, d\phi \, d\theta. \tag{3}$$

The kinetics of TiO_2-based photocatalytic reactions is always a function of the rate of photon absorption in the TiO_2 photocatalyst. Depending on the type of photocatalytic reactor under analysis, the rate of photon absorption may be expressed per unit reactor irradiated volume or per unit reactor irradiated photocatalytic surface. When modeling slurry type of photocatalytic reactors, where the TiO_2 fine powder is suspended in the reactive medium, the system could be assumed as pseudo-homogeneous, and the rate of photon absorption can be expressed per unit reactor volume. Under such conditions, the kinetics of photocatalytic reactions can be expressed as a function of the local volumetric rate of photon absorption (LVRPA or $e^{a,V}$),[22] where:

$$e_\lambda^{a,V}(\mathbf{x}) = \kappa_\lambda(\mathbf{x}) G_\lambda(\mathbf{x}). \tag{4}$$

In Eq. 4, κ_λ is the effective spectral volumetric absorption coefficient of the photocatalytic medium, which consists of the TiO_2 particles and the reacting medium, considered in this case as pseudohomogeneous system comprised the TiO_2 particles and an aqueous medium. Consequently, this parameter, κ_λ, is a function of the TiO_2 concentration, the pH, the shape and size of the particles, and size of the particle agglomerates and needs to be evaluated experimentally by using special spectrophotometric techniques.[23]

On the other hand, when modeling a reactive wall photocatalytic reactor or a fixed-bed photocatalytic reactor, in which a thin layer of TiO_2 is coated on the surface of an inert support, it seems to be more appropriate to refer the photon absorption rate per unit area of irradiated TiO_2-coated surface. Therefore, the local surface rate of energy absorption (LSRPA or $e^{a,S}$) is defined as follows:

$$e_\lambda^{a,S}(\mathbf{x}) = \int_{t_k=0}^{t_{k,TiO_2}} \alpha_\lambda(\mathbf{x}) \, G_\lambda(\mathbf{x}) dt_k = q^i(\mathbf{x}) - q^t(\mathbf{x}), \tag{5}$$

where $\alpha_\lambda(\mathbf{x})$ is the spectral volumetric absorption coefficient of pure TiO_2 (calculated or measured), $q^i(\mathbf{x})$ and $q^t(\mathbf{x})$ are the local net radiation fluxes incident on the TiO_2 films and the local net radiation fluxes transmitted through them (Figure 5a), respectively, and t_{k,TiO_2} is the thickness of the TiO_2 films.

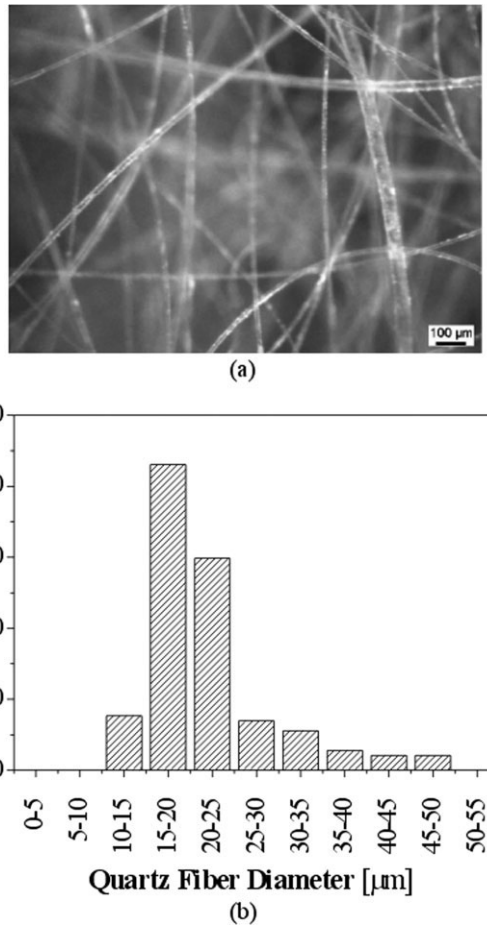

Figure 4. (a) Micrograph of the quartz wool; (b) histogram of the diameter distribution of the quartz wool.

Finally, it is possible to relate the total rate of photon absorption in the reactor to the local rate of photon absorption, which can be referred to the reactor volume ($e^{a,V}$) or to the photocatalytic surface ($e^{a,S}$). They are two different functions; however, it can be shown that:

$$\int_{V_{\text{reactor}}} e_\lambda^{a,V}(\mathbf{x}) dV = \int_{S_{\text{reactor}}} e_\lambda^{a,S}(\mathbf{x}) dS, \tag{6}$$

where V_{reactor} is the total reactor volume and S_{reactor} is the total photocatalytic surface of the reactor.

Radiation modeling description

The physical events considered by the radiation model are represented in Figure 5. Photons with different energies (i.e., with different wavelengths) and different propagation directions are emitted by the lamp, but only a fraction of them can reach the reactor windows. Those photons that reach the reactor windows may be partially reflected on its surface, partially absorbed by the borosilicate glass of the windows, or partially transmitted toward the reactor interior, where the TiO_2-coated wool is placed. Similarly, photons traveling

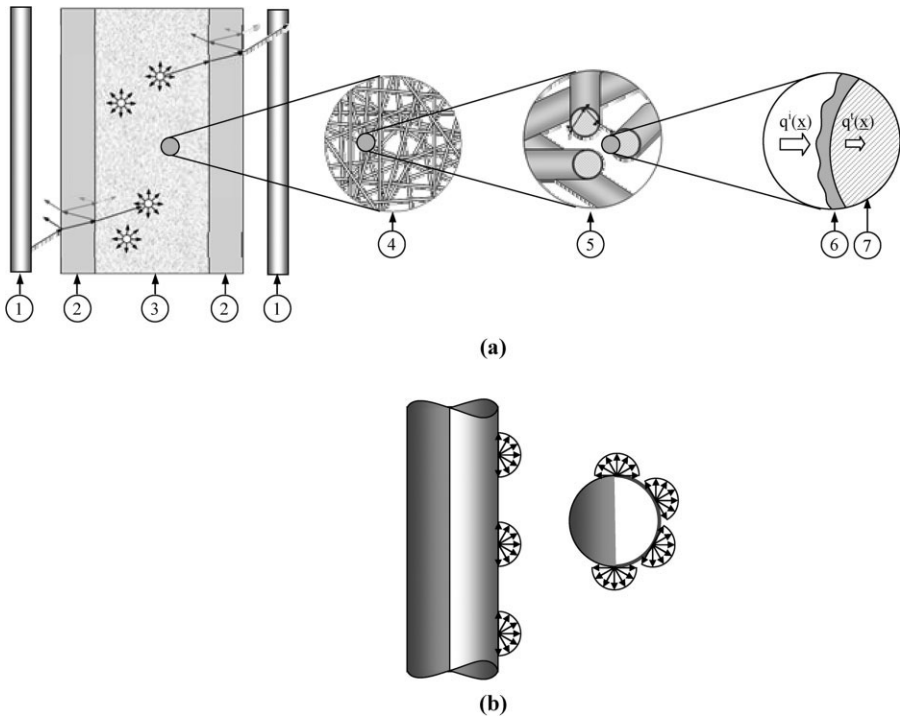

Figure 5. Schematic representation of the (a) photocatalytic reactor and (b) lamp emission.

(1) UV lamps, (2) borosilicate windows, (3) TiO_2-coated quartz wool, (4) detailed representation of the TiO_2-coated quartz wool, (5) TiO_2-coated quartz fibers, (6) TiO_2 film, (7) quartz fiber.

inside the reactor will follow a straight line until they reach a TiO_2-coated fiber, where they can be reflected, absorbed in the TiO_2 films, or transmitted. Interactions of photons with the TiO_2-coated quartz wool are more complex to model, because photons are subjected to a more intricate series of events that involves single and multireflections on the TiO_2 films of different fibers, multireflections inside a single quartz fiber, and multirefraction on the water/quartz and quartz/water interfaces. Moreover, the cylindrical geometry increases even more the existing difficulties. Finally, photons traveling inside the reactor can reach the reactor windows. In such case, they can be reflected, partially absorbed by the borosilicate glass, or transmitted through the reactor windows.

As mentioned earlier, from a kinetic point of view, it is necessary to evaluate the photon absorption rate in the TiO_2 films. Furthermore, to validate the radiation model, it is also necessary to evaluate the effective transmittance of the reactor, because neither the $e^{a,V}$ nor the $e^{a,S}$ can be actually measured experimentally without disturbing the existing radiation field. Consequently, by means of the available information concerning the different optical properties and an ad hoc FORTRAN program, based on the solution algorithm schematically shown in Figure 6, the global transmittance of the reactor was predicted for the model validation. The calculations were done with a 1.60-GHz Pentium III Processor, and the time required for a typical run, considering 10^5 photons (for the four lamps), was on the order of 20 min. Then, the $e^{a,S}$ in the TiO_2 was evaluated to analyze the radiation distribution and the existence of a uniform or nonuniform distribution of absorbed photons inside the reactor.

Model development and assumptions

The Monte Carlo, Photocatalytic Packed-bed Radiation model (MCPPR model) was developed considering the following assumptions:

(i) Photons are emitted individually, where its emission point on the lamp surface ($\mathbf{x}_{ph,i}$), propagation direction ($\mathbf{x}_{di,i}$), and wavelength (λ_i) are stochastically defined considering the particularities of the employed lamps. Because the lamps have an internal reflector on half of their emitting surface, they emit with a preferential orientation (Figure 2b) and neither of the well-known radiation emission models, such as the Line Source with Spherical Emission model,[24,25] the Line Source with Diffused Emission model,[26,27] the Extended Source with Volumetric Emission model,[22,28] nor the Extended Source with Surface Emission model[22,29] can be used to properly estimate the radiation emission by the employed lamps. To take into account the particularities of the lamps, photons are considered to be emitted from half of the surface of the lamp opposite to the reflector (Figure 5b), whose direction of superficial emission is assumed isotropic, and whose wavelength is defined in agreement with the particular spectral emission of the employed lamps (Figure 2a). The effective emission flux on the lamp surface was calculated from experimental measurements as described earlier.

(ii) Photon tracking is based on the laws of geometrical optics:

$$\mathbf{x}_{ph,i} = \mathbf{x}^*_{ph,i} + \xi \mathbf{x}_{di,i} \tag{7}$$

where the variable ξ represents a plausible distance that the photon can travel without reaching the reactor windows or

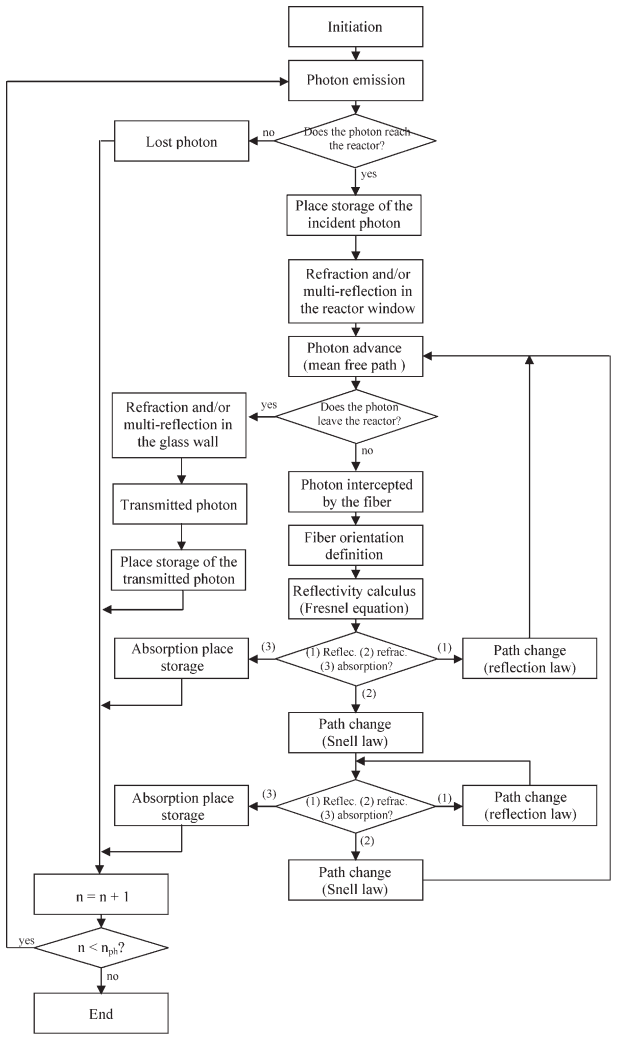

Figure 6. Simplified approach using Monte Carlo algorithm.

any quartz fiber, and the asterisk refers to the previous location of the photon.

(iii) Those photons emitted by the lamp that do not reach the reactor window are considered lost, and a new photon is emitted.

(iv) On the other hand, those photons that reach the reactor window can be reflected or refracted. The angle-dependant local reflectivity is calculated using the Fresnel equation[30]:

$$\rho(\mathbf{i},\mathbf{t},\mathbf{n}_{\text{loc}})=\frac{1}{2}\left[\frac{\mathbf{n}_1(\mathbf{n}\cdot\mathbf{i})-\mathbf{n}_2(\mathbf{n}\cdot\mathbf{t})}{\mathbf{n}_1(\mathbf{n}\cdot\mathbf{i})+\mathbf{n}_2(\mathbf{n}\cdot\mathbf{t})}\right]^2+\frac{1}{2}\left[\frac{\mathbf{n}_1(\mathbf{n}\cdot\mathbf{t})-\mathbf{n}_2(\mathbf{n}\cdot\mathbf{i})}{\mathbf{n}_1(\mathbf{n}\cdot\mathbf{t})+\mathbf{n}_2(\mathbf{n}\cdot\mathbf{i})}\right]^2 \tag{8}$$

where **i** and **t** are the propagation direction of the incident photon and of the transmitted photon, respectively, and **n** is the normal vector to the surface. Each photon is stochastically assigned to be specularly reflected or specularly refracted considering a random number and the reflectivity.

(v) When a photon is reflected, the new direction of propagation is given by the vectorial equation:

$$\mathbf{n}\times\mathbf{i}=(\mathbf{n}\times\mathbf{r})\;;\quad \mathbf{r}\neq\mathbf{i} \tag{9}$$

where **r** is the direction of the reflected photon. Those photons that are reflected at the entrance window are considered lost, and a new photon is emitted.

(vi) When a photon is refracted, its propagating direction changes because the refractive indexes of the two propagating media are different (i.e., air to borosilicate glass, borosilicate glass to water, water to TiO_2, TiO_2 to quartz, etc.). The new direction of the refracted photon is evaluated using the Snell law[30]:

$$\mathbf{n}\times\mathbf{i}=\frac{\mathbf{n}_1}{\mathbf{n}_2}(\mathbf{n}\times\mathbf{t});\quad \mathbf{i}\neq\mathbf{t}\;\frac{\mathbf{n}_1}{\mathbf{n}_2} \tag{10}$$

where **n** is the normal vector to the interface of the mediums 1 and 2 at the interception point.

(vii) Once inside the borosilicate glass window, photons can be absorbed, transmitted, or internally reflected. The trajectories of photons in the reactor windows are computed until they are absorbed (lost photons) or leave off the region under analysis. Besides, multireflection of photons inside the reactor windows is considered. Then, photons can abandon the window with one direction that implies either to go away from the reactor (lost photon) or enter back into the quartz wool filling.

(viii) The photocatalyst consists of a great number of TiO_2-coated quartz fibers, which are uniformly distributed in the reactor. Taking into account the reactor dimensions described in Table 1 and its very small average thickness/height and thickness/width ratios (0.010 and 0.052, respectively), the fiber orientations are considered as follows: the axis of each fiber is assumed parallel to the reactor windows and its angle with respect to the z coordinate is randomly assigned. Under such considerations, it is not important whether or not the fibers are straight or curved, as long as they remain in the same plane, i.e., parallel to the windows.

(ix) The mean free path of photons inside the reactor was estimated considering the probability for a traveling photon to reach the fibers. The diameter distribution of the quartz fibers used is shown in Figure 4b, where it can be noted that the thickness of the fibers is not uniform. For this reason, the total sum of projected area of the fibers was calculated by

$$A^{\text{long}}_{\text{fiber,T}}=\sum_{i=1}^{n_{\text{T}}}A^{\text{long}}_{\text{fiber,i}}=\sum_{i=1}^{n_{\text{T}}}2L_{\text{fiber},i}\quad R_{\text{fiber},i} \tag{11}$$

where $L_{\text{fiber},i}$ and $R_{\text{fiber},i}$ are the length and radius of the ith quartz fiber, respectively, and n_{T} is the total number of fibers that comprises the reactor filling. Since the values of n_{T} and $L_{\text{fiber},i}$ cannot be obtained experimentally, Eq. 11 is expressed as a function of variables that can be readily obtained (Appendix A):

$$A^{\text{long}}_{\text{fiber,T}}=\frac{2\,M_{\text{fiber}}}{\rho_{\text{quartz}}\,\pi}\,\frac{\sum_{R=R_{\min}}^{R_{\max}}n_{\text{R}}\,R_{\text{fiber}}}{\sum_{R=R_{\min}}^{R_{\max}}n_{\text{R}}\,R^2_{\text{fiber}}}, \tag{12}$$

where M_{fiber} is the mass of quartz fibers placed in the reactor, ρ_{quartz} is the quartz density, $R_{\min}$ and $R_{\max}$ represent the minimum and maximum radius of the fibers respectively,

and n_R is the number of fibers whose radius is R_{fiber}, information that can be obtained from the diameter distribution of the quartz fibers (Figure 4b).

The inverse of the mean free path of photons inside the reactor was estimated as the total sum of the projected area of the fibers divided by the volume they occupy in the reactor, i.e., the reactor volume:

$$\mathrm{MFP}^{-1} = \frac{A_{\mathrm{fiber,T}}^{\mathrm{long}}}{V_{\mathrm{reactor}}} \tag{13}$$

where MFP is the mean free path.

(x) The plausible photon advance inside the reactor is stochastically estimated by

$$\xi = -\mathrm{MFP}\,\ln(R), \tag{14}$$

where the variable ξ represents a plausible distance that the photon can travel without reaching any fiber and R is a uniformly distributed random number. Again, the photon advance is calculated with Eq. 7.

(xi) When the position of the photon, estimated according to Eq. 7, is inside the reactor filling, the photon is considered to reach a quartz fiber. Otherwise, the photon is considered to reach the reactor windows and the location where the photon reaches the window is evaluated.

(xii) Those photons that reach the quartz fibers, which are coated with TiO_2, can be partially reflected on the surface, partially attenuated by the TiO_2, and partially refracted toward the interior of the quartz fiber. Again, the angle-dependent local reflectivity is calculated using the Fresnel equation (Eq. 8), and the effective transmittance of the TiO_2 films is evaluated by considering the spectral volumetric absorption coefficient of pure TiO_2 and the average thickness of the film.

(xiii) The spectral volumetric absorption coefficient of the TiO_2 is a strong function of the wavelength, and their numerical values in the range of emission of the lamp (340–420 nm) were calculated by using the correlation proposed by Sodergren et al.[31]:

$$\alpha_\lambda = \exp(29 - 85\,\lambda), \tag{15}$$

where α_λ is the spectral volumetric absorption coefficient of the TiO_2 in μm^{-1}, and λ is the wavelength in μm.

(xiv) The average thickness of pure TiO_2 films was estimated by considering that all the TiO_2 is uniformly distributed on the total available surface of the quartz wool fibers. The numerical value was calculated by considering the mass and the density of TiO_2 immobilized on the fibers (M_{TiO_2} and ρ_{TiO_2}, respectively), the mass and the density of the fibers (M_{fiber} and ρ_{quartz}, respectively), and the fiber diameter distribution (Appendix B):

$$t_{k,TiO_2} = \frac{M_{TiO_2}\,\rho_{quartz}}{2\,M_{fiber}\,\rho_{TiO_2}} \frac{\sum_{R=R_{min}}^{R_{max}} n_R\,R_{fiber}^2}{\sum_{R=R_{min}}^{R_{max}} n_R\,R_{fiber}}. \tag{16}$$

The resulting value was $t_{k,TiO_2} = 0.687\ \mu$m.

(xv) Photons traveling inside the quartz fiber are not absorbed because the spectral volumetric absorption coefficient of quartz in the wavelength range of the radiation emitted by the lamps is negligible.

(xvi) However, photons traveling inside the quartz fiber can be reflected on the internal surface of the fiber, the effect that was taken into account in the MCPPR model. Photons reflected on the TiO_2 films or transmitted through the fibers continue their interaction with the fiber, until they are either absorbed in the TiO_2 coatings or leave the interior of the reactor.

In general terms, photons are tracked until they are either absorbed by the TiO_2 films, absorbed in the borosilicate glass of the reactor windows, or until they leave the reactor. The algorithm permits to evaluate the $e^{a,S}$ in the TiO_2 films and the local net spectral radiation flux on the inner and on the outer reactor windows. In this way, when a photon is absorbed in the TiO_2 film, the absorption place is stored in a matrix that corresponds to the discretized reactor volume. This matrix, with the information of the absorption position of all photons, is used to calculate the $e^{a,S}$ in the reactor:

$$e^{a,S}(x,y,z) = n_{ph,absorbed}(x,y,z)\,\frac{n_{lamp}\,P_{eff}}{n_{ph,T}\,\Delta x\Delta y\Delta z}\,\frac{V_{reactor}}{S_{reactor}}, \tag{17}$$

where $n_{ph,absorbed}(x,y,z)$ is the number of photons absorbed in the element corresponding to the coordinates (x, y, z), n_{lamp} is the number of lamps and P_{eff} is the emission power of each lamp, $n_{ph,T}$ is the total number of photons considered in the MC method, and $\Delta x\Delta y\Delta z$ is the volume of each element. Similarly, when a photon reaches the reactor or is transmitted through it, the place where the photon reaches or leaves the reactor windows is stored in a matrix that corresponds to the discretized window surfaces. The spectral local net radiation flux at the inlet and outlet windows are evaluated as follows:

$$q_{in,\lambda}(x,z) = n_{ph,inlet\ wall,\lambda}\,\frac{n_{lamp}P_{eff,\lambda}}{n_{ph,T}\,\Delta x\Delta z} \tag{18}$$

$$q_{out,\lambda}\,(x,z) = n_{ph,outlet\ wall,\lambda}\,\frac{n_{lamp}P_{eff,\lambda}}{n_{ph,T}\,\Delta x\Delta z} \tag{19}$$

where $n_{ph,inlet\ wall}$ and $n_{ph,outlet\ wall}$ are the number of photons that reach the inner and outer windows, respectively. Finally, the local net radiation flux at the inlet and outlet windows are evaluated considering the spectral fluxes (Eqs. 18 and 19) at the wavelengths emitted by the lamp, which were pondered according to the spectral sensitivity of the radiometer.

$$q_{in,rad}(x,z) = \sum_{\lambda=340\ nm}^{420\ nm} q_{in,\lambda}(x,z) f_{radiom}(\lambda) \tag{20}$$

$$q_{out,rad}(x,z) = \sum_{\lambda=340_{nm}}^{420_{nm}} q_{out,\lambda}(x,z) f_{radiom}(\lambda) \tag{21}$$

where $f_{radiom}(\lambda)$ is the spectral sensitivity of the radiometer (information provided by the radiometer manufacturer).

Model Validation

The radiometric measurement sets of the radiation flux that reaches the reactor windows and the radiation flux that is transmitted through the reactor were used for estimating

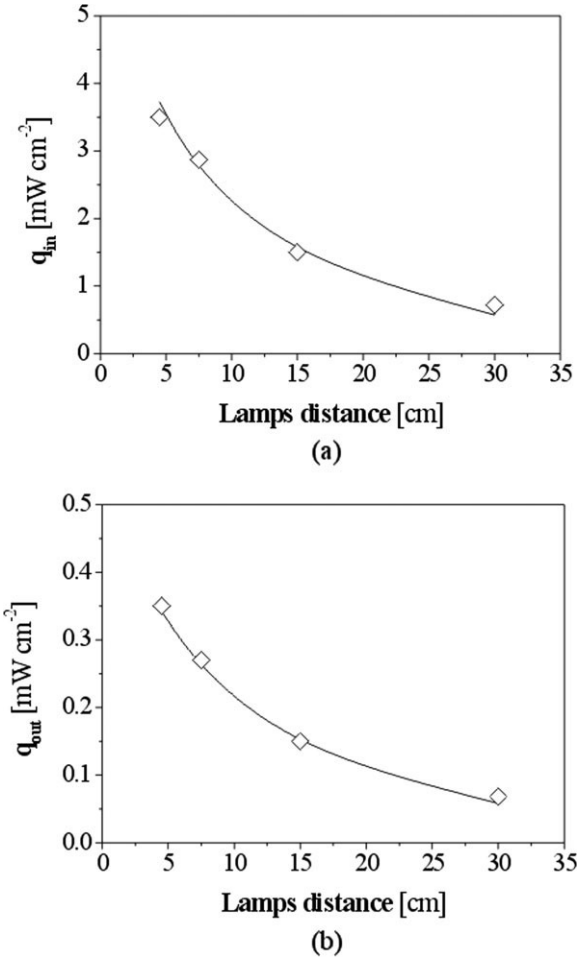

Figure 7. Average values of the (a) net radiation flux reaching the reactor window ($y = 0$) and (b) net radiation flux transmitted through the opposite window of the reactor ($y = 1$ cm).

Keys in (a): (◇) experimental data, (—) values predicted by the lamp emission model. Keys in (b): (◇) experimental data, (—) values predicted by the radiation model of the reactor.

the effective power of the lamps and to validate the proposed radiation model, respectively.

In Figure 7a, the mean values of the measurements of the incident photon flux on one of the reactor window entrances are reported for different lamp distances from this reactor window. As expected, the farther the lamps are from the reactor window, the lower is the photon flux reaching such window. Consequently, the irradiation level of the reactor can be easily modified only by changing the distance of the lamps from the reactor. The effective power emission of the lamps (P_{eff}) represents essential information to be used as a boundary condition in radiation model. Its numerical value was estimated from the incident fluxes reaching the reactor window. In other words, knowing the radiation reaching the reactor walls allowed us to calculate the effective emission power of the lamps. This parameter was adjusted to minimize the sum of the square of the differences between the model predictions of the incident radiation fluxes and the collected experimental information. The obtained result of the effective power emission of the lamps is shown in Table 1 ($P_{\text{eff}} = 3.25 \pm 0.33$ W). In Figure 7a, the estimated values of the incident photon flux were included, showing that the adjusted emission model that provided the estimated lamp power boundary condition is capable of properly describing the influence of the lamp distance on the incident radiative fluxes arriving on the reactor window.

Similarly, Figure 7b shows the experimental values and the model predictions of the net radiation flux on the reactor window opposite to the lamps. These data represent the radiation transmitted through the reactor. This radiation flux results from the interaction of the radiation that reaches the entrance window with such window (where photons are partially reflected, transmitted, absorbed in the borosilicate glass, etc.), with the reactor filling (where photons are partially reflected on the fibers, absorbed in the TiO_2 coatings, undergo internal multireflections in the quartz fibers, etc.), and with the reactor outlet window (where the same effects as those in the reactor entrance window take place). Figure 7b shows the predictions obtained using the developed model, providing a good agreement with the experimental results. The root mean square error between model predictions and experimental data was smaller than 9.7%.

From the experimental data presented in Figures 7a,b, it can be also concluded that the effective transmittance of the reactor, defined as the ratio of the incident (Figure 7a) and transmitted net radiation flux (Figure 7b), is about 10%, independently of the distance of the lamps from the reactor.

Figure 8 gives a representation of the local net radiation flux that reaches the entrance window of the reactor (i.e., $y = 0$). It can be observed that the radiation field is almost uniform along the x and z coordinates at the surface of the reactor window.

Regarding the desirable uniformity of the radiative energy distribution along the y coordinate, Figure 9a shows the LSRPA profiles vs. the thickness of the reactor. Notwithstanding that the reactor thickness is very small and the TiO_2 film thickness is very thin, the isoactinic condition has not been completely achieved and at the center of the reactor, the value of the radiation field, expressed in terms of the radiation absorption property $(e^{a,S})$, has been reduced in approximately

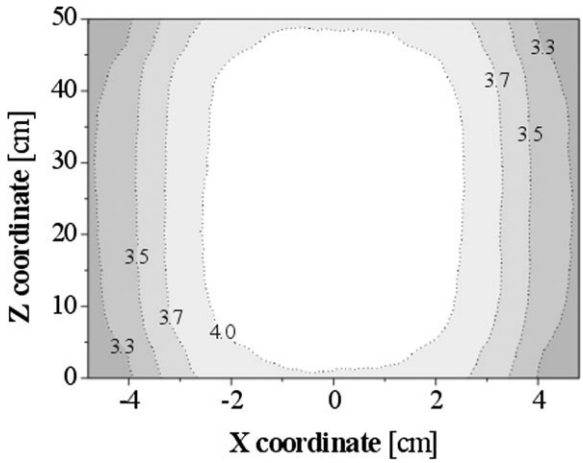

Figure 8. Local net radiation flux at the entrance window (units: mW cm^{-2}).

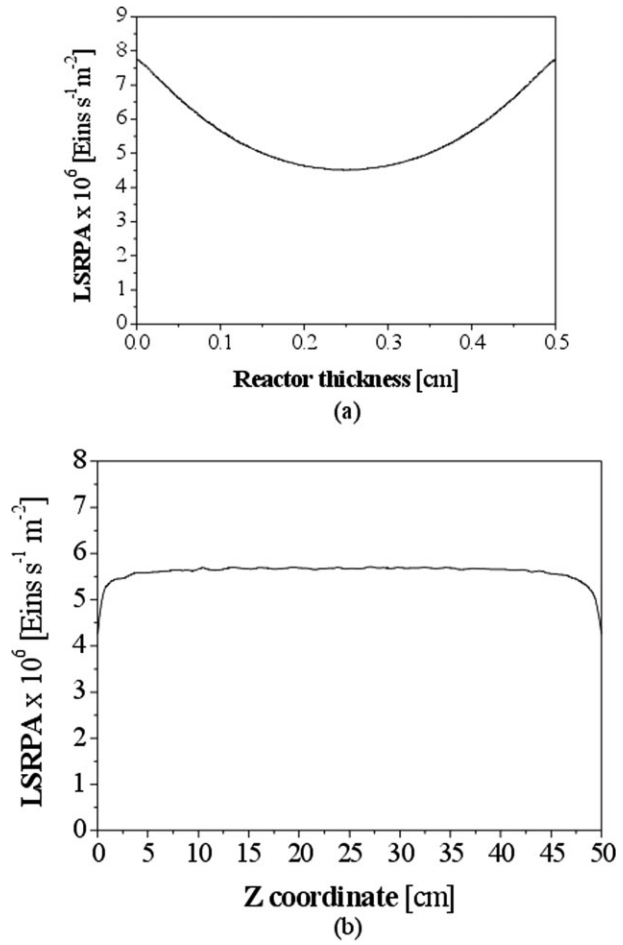

Figure 9. LSRPA profiles inside the reactor as a function of the (a) *y* coordinate and (b) *z* coordinate.

41%. Consequently, not very large reactors in the characteristic direction of radiation propagation could be expected to be very effective, because after a few centimeters, the central part of the reactor would be useless (because of the lack of activating radiative energy). In this regard, Brucato et al.[19] proposed the use of the plane slab reactor irradiated from both sides as a suitable configuration to increase the uniformity of the radiative energy distribution. The results obtained in this article are in agreement with those obtained by Brucato et al.,[19] confirming that building photocatalytic reactors with the mentioned restrictions in their geometry permits the reduction of dark regions inside the reactor.

Figure 9b shows the rate of photon absorption distribution along the *z* coordinate, which is coincident with the axial direction of the lamps (Figure 1). Regardless of the fact that the lamp length is larger than the reactor length, the end effects can still be observable. This result is in agreement with the fact that the emitted radiation is divergent and consequently, as a general case, the radiation flux in a given point is a function of the distance between this point and the lamp axis and also of the longitudinal coordinate (i.e., the *z* coordinate). However, in this case, the end effects are not very important due to the already mentioned differences between the lamp and the reactor lengths.

Parametric Analysis

Regarding the radiative energy distribution, the ideal situation for photocatalytic reactors is that in which all the photons reaching the reactor are uniformly absorbed on a large surface of TiO_2 in contact with the reactants. However, in real photocatalytic reactors, a quite significant percentage of photons may be reflected on the reactor windows, another percentage may be absorbed by other components of the reactor or transmitted through the reactor, and the remaining percentage is actually absorbed in the TiO_2 films. In this sense, the greater the percentage of photons absorbed in the TiO_2 films, the more effective will be the use of the radiation for conducting photocatalytic reactions. Besides, radiative energy nonuniformities are irreducible in a participative medium, which is the common case in photocatalytic applications. Excessive gradients of the irradiation level in the reactor are undesirable because some regions of the reactor will be over illuminated, which may generate mass transfer resistances, and the rest of the reactor will remain in almost dark conditions, which will be inefficient for the photocatalytic reactions. Consequently, the existence of significant gradients of LSRPA in photocatalytic reactors tends to reduce the reactor efficiency.

In this section, a parametric analysis of the radiation field in the TiO_2-coated quartz wool reactor is presented, where the effect of TiO_2 loading (M_{TiO_2}), quartz wool loading (M_{fiber}), and quartz fiber radius (R_{fiber}) on the radiation field is discussed. To analyze the radiation absorption nonuniformities inside the reactor, the LSRPA profiles against the reactor thickness obtained under different conditions are represented in Figures 10a, 11a, and 12a. To analyze the photon usage efficiency, the percentage of photons absorbed in the TiO_2 films, transmitted through the reactor, absorbed in the borosilicate glass of the reactor windows, and leaving the reactor due to reflection or out scattering are represented by the bar diagrams in Figures 10b, 11b, and 12b.

Influence of the TiO_2 loading immobilized on the quartz wool on the LSRPA

The influence of the titanium dioxide loading on the quartz wool on the radiation absorption profiles is shown in Figure 10a, and the corresponding distribution of photon ending is represented in Figure 10b. The following TiO_2 loading values were used for the parametric analysis: 1, 5, 10, 20% TiO_2 w/w. Constant values of the quartz wool mass ($M_{wool} = 17.2$ g) and quartz fiber radius ($R_{fiber} = 12$ μm) were used. The value of the photocatalytic surface results approximately 1 m^2 for all the cases considered in this subsection.

The increment of the TiO_2 loading mainly enhances the absorption of photons in the TiO_2 films (Figure 10b), and therefore increases the corresponding values of LSRPA (Figure 10a).

For low percentages of TiO_2 loading, the predicted values of LSRPA are low and almost uniform throughout the reactor volume. For example, unimportant variations of the energy absorption rate are observed when the TiO_2 loading is 1% w/w, and therefore an isoactinic reactor behavior may be assumed. Besides, the values of LSRPA are very low (smaller than 1.0×10^{-6} Einstein s^{-1} m^{-2}), which is a

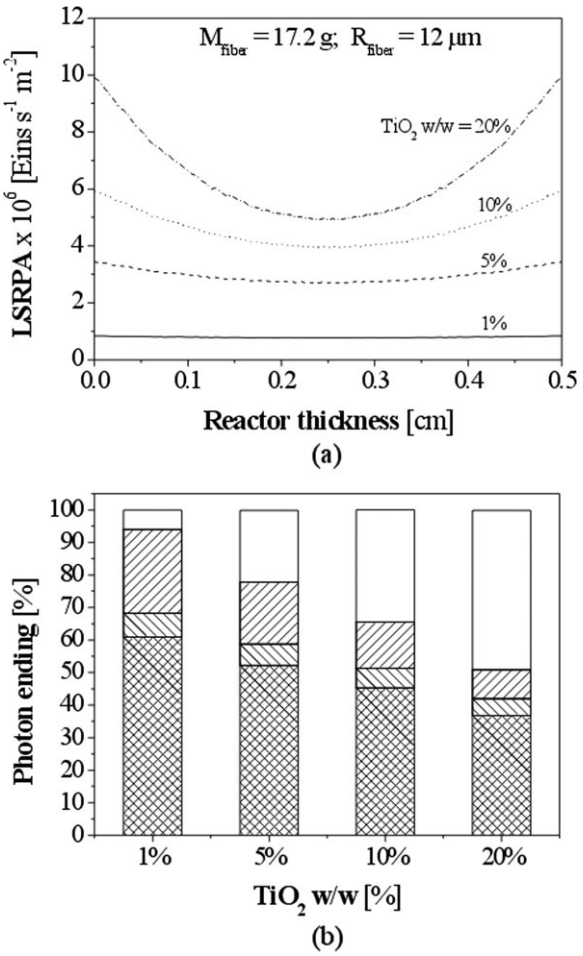

Figure 10. (a) Parametric LSRPA profiles corresponding to variation in the mass of immobilized TiO_2. (b) Distribution of photon ending for different TiO_2 mass values.

(□) percentage of photons absorbed in the TiO_2 films, (▨) percentage of photons transmitted through the reactor, (▩) percentage of photons absorbed in the borosilicate glass of the reactor windows, (▩) percentage of photons leaving the reactor because of reflection or out scattering.

consequence of the low percentage of photons that are absorbed in the TiO_2 coatings (6%). There is a great percentage of photons that leaves the reactor without being absorbed (87%), as a consequence of those photons that are transmitted through the reactor (26%) and those photons that leave the reactor due to either reflection or out scattering (61%). Under these conditions, very likely, the reaction rate of photocatalytic reactions will be very low because of the reduced irradiation level.

On the other hand, for high photocatalytic loadings, the LSRPA in the entire reactor is much greater, particularly in those regions close to the windows (Figure 10a). For example, when the TiO_2 loading is 20% w/w, the mean value of the LSRPA obtained is 6.6×10^{-6} Einstein s^{-1} m^{-2} and the radiation absorption gradient is noticeable. The value of LSRPA at the center of the reactor is 50% lower than the corresponding LSRPA on the windows. Even though, the values of LSRPA in every region of the reactor are higher than those obtained with lower loading of TiO_2. In this case, about 50% of the photons are absorbed in the TiO_2 films (Figure 10b). If no mass transfer limitations appear and the irradiation levels are not too high, increasing the TiO_2 loading on the fiber surface would have a positive effect on the photocatalytic reactor behavior.

Influence of the quartz fiber wool loading on the LSRPA

Figure 11a represents the results of changing the quartz fiber wool loading inside the reactor volume, and Figure 11b illustrates the corresponding distribution of photon ending. Six values of the quartz fiber wool loading were investigated: 1, 5, 10, 17.2, 50, and 100 g. The TiO_2 loading on the quartz wool is 14.4% w/w and the quartz fiber radius is 12 μm. It is important to consider in the current analysis that the total amount of TiO_2 in the reactor and the photocatalytic surface linearly increase with the increment of the packing loading.

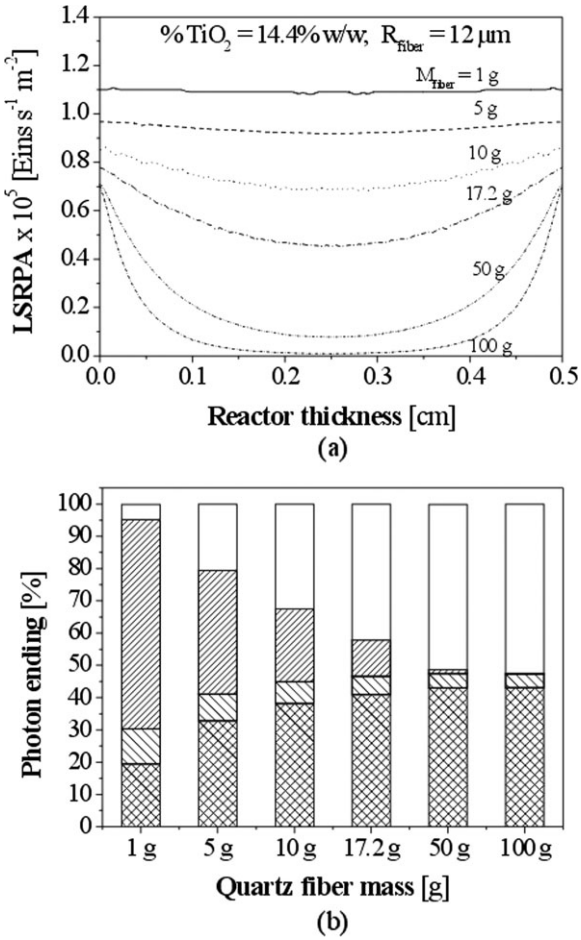

Figure 11. (a) Parametric LSRPA profiles corresponding to variation in the mass of the quartz fiber wool. (b) Distribution of photon ending for different quartz wool mass.

(□) percentage of photons absorbed in the TiO_2 films, (▨) percentage of photons transmitted through the reactor, (▩) percentage of photons absorbed in the borosilicate glass of the reactor windows, (▩) percentage of photons leaving the reactor because of reflection or out scattering.

The increase in the quartz fiber loading with a constant TiO_2 percentage mainly enhances the absorption of photons in the TiO_2 films (Figure 11b) and reduces the mean value of LSRPA (Figure 11a). When the mass of quartz fiber wool in the reactor is low, for example equal to 1 g, the mean value of the LSRPA is high (1.1×10^{-5} Einstein s^{-1} m^{-2}, Figure 11a) and the percentage of photons that are absorbed in the TiO_2 films is low (4.7%, Figure 11b) because of the small photocatalytic area of the reactor. However, insignificant spatial variations of the LSRPA are observed due to the low radiation attenuation generated in this loose packing. The final consequence is that filling the reactor with a very low packing loading generates an unfavorable situation because of the low radiation usage and the small photocatalytic area. Besides, because of the increment of the LSPRA at low values of packing loading (Figure 11a), mass transfer limitations may appear.

Nevertheless, when the quartz wool loading is large ($M_{wool} = 100$ g), the profile of LSRPA along the thickness of the reactor is highly nonuniform and the value of the radiation absorption property is almost null at the center of the reactor. This effect is undesirable because most of the reactor will remain in dark conditions.

Because of the fact that the use of both low and high loading of quartz wool will have negative consequences on the radiation field, an intermediate value should be preferred. In this work, the value of 17.2 g was selected because the gradients of the irradiation level are quite smooth, and the percentage of photon absorption in the TiO_2 films is high enough.

Influence of the quartz fiber radius on the LSRPA

Figure 12a presents a plot of the parametric LSRPA profiles corresponding to different values of the quartz fiber radius, and Figure 12b shows the corresponding distribution of photon ending. In this parametric study, four values of the quartz fiber radius (5, 12, 50, and 100 μm), and constant values of the TiO_2 loading (14.4%) and quartz fiber wool loading (17.2 g) were investigated. Even when the quartz fiber loading is constant in all the cases considered in this subsection, the available photocatalytic areas differ in each case because of the fiber radius modification. Similarly, in spite of the fact that the amount of TiO_2 remains invariable, the thickness of the TiO_2 films will increase with the increment of the fiber radius as a consequence of the reduction of the photocatalytic surface.

According to modeling results, the quartz fiber radius has no fundamental effect on the uniformity of the irradiation level in the reactor (Figure 12a) or on the ability of the TiO_2 existing in the bed to absorb radiation (Figure 12b). However, the numerical values of the LSRPA dramatically changes for the different values of the fiber radius analyzed.

When very thin fibers are considered, the LSRPA is significantly low (approximately 2.5×10^{-6} Einstein s^{-1} m^{-2} for $R_{fiber} = 5$ μm); but in this case, the catalyst surface area for reaction is appreciably large ($\sim$2.6 m^2). This situation may result in an improvement in the reactor performance because of the increment of the photocatalytic area, which contributes to the reduction of possible mass transfer limitations.

Conversely, when the fiber radius is too large, the LSRPA is high (approximately 3.75×10^{-5} Einstein s^{-1} m^{-2} for $R_{fiber} = 100$ μm), and the catalyst surface area is very low ($\sim$0.13 m^2). This situation would generate an undesirable effect on the reactor performance because mass transfer limitations would be present.

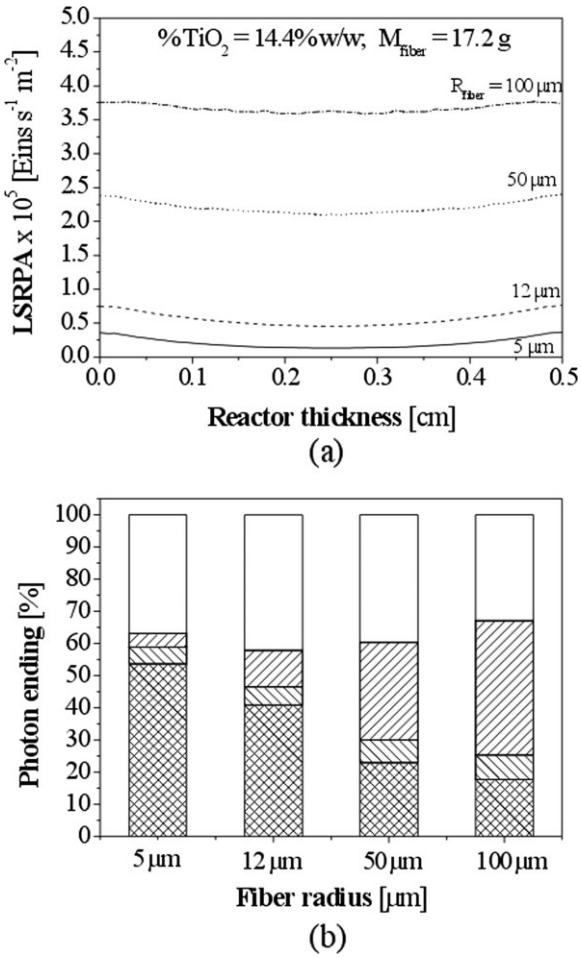

Figure 12. (a) Parametric LSRPA profiles corresponding to variation in the radius of the quartz fiber. (b) Distribution of photon ending for different fiber radius.

(□) percentage of photons absorbed in the TiO_2 films, (▨) percentage of photons transmitted through the reactor, (▧) percentage of photons absorbed in the borosilicate glass of the reactor windows, (▩) percentage of photons leaving the reactor because of reflection or out scattering.

In this respect, the information that can be obtained from a radiation model may be very useful for any future reactor design because it imposes a trade-off decision. It may be worth mentioning that with a complete different approach and for a different application, Ref. 19 reports some conclusions that in some instances are qualitatively similar to the ones obtained in this work.

Conclusions

Starting from first principles and using a MC approach, the radiation field of a flat, packed-bed, photocatalytic reactor made of titanium dioxide-coated quartz fiber wool,

irradiated from both sides was modeled and experimentally validated. The proposed radiation model considers a series of coupled events that takes places when radiation reaches the reactor, such as the radiation reflection and refraction on/in the reactor windows, the photon absorption in the TiO_2 coatings, and the interaction with the fibers. The model was evaluated by comparing the predicted values of the transmitted radiation fluxes with those obtained from experiments. A good agreement was observed, the root mean square error being $<9.7\%$.

From the results of the parametric analysis, it was possible to conclude that:

(1) Under not too high irradiation levels (to avoid mass transfer limitations), high TiO_2 loading on the fiber surface would have a positive effect on the photocatalytic reactor behavior due to the increment of the photon absorption in the TiO_2.

(2) Filling the reactor with a very low quartz fiber loading may generate an unfavorable situation because of the low radiation usage. Similarly, filling the reactor with a very high quartz fiber loading is also undesirable because most of the reactor may remain in dark conditions. An intermediate value of fiber loading should be selected.

(3) The performance of TiO_2-coated fiber reactors may be improved when very thin fibers are used as the support for TiO_2, because increasing the photocatalytic area may contribute to the reduction of possible mass transfer limitations.

This radiation model could be used to design a photocatalytic reactor to improve the radiative energy distribution or could be coupled with intrinsic reaction kinetic models to describe the performance of the photocatalytic degradation reaction of water or air pollutants.

Acknowledgments

The authors are grateful to INCA "Consorzio Interuniversitario La Chimica per l'Ambiente" on Legge 488 funds, Research Project 3: "Rimozione di inquinanti mediante processi a membrana e fotocatalitici," Universidad Nacional del Litoral (UNL), Consejo Nacional de Investigaciones Científicas y Técnicas (CONICET), and Agencia Nacional de Promoción Científica y Tecnológica (ANPCyT) for their financial support. They also thank Eng. Salvatore Castellana for his participation in some parts of the experimental work.

Notation

A = surface, cm^2
$e^{a,S}$ = local surface rate of photon absorption, Einstein s^{-1} m^{-2}
f_{radiom} = spectral sensitivity of the radiometer, dimensionless
G = incident radiation, mW cm^{-2}
$\mathbf{i}$ = propagation direction of the incident photon, dimensionless
I = specific radiation intensity, mW cm^{-2} sr^{-1}
L = length, cm
M = mass, mg
MFP = mean free path, cm
n = refractive index relative to air, dimensionless; also number of photons or lamps, dimensionless
P_{eff} = effective emission power of the lamp, W
q = local net radiation flux, mW cm^{-2}
R = radius, cm; also uniformly distributed random number, dimensionless
$\mathbf{r}$ = propagation direction of the reflected photon, dimensionless
t_k = average thickness of the TiO_2 films, μm
$\mathbf{t}$ = propagation direction of the transmitted photon, dimensionless
w = mass percentage, dimensionless
x = rectangular coordinate, cm
y = rectangular coordinate, cm
z = rectangular coordinate, cm

Greek letters

$\boldsymbol{\alpha}$ = volumetric absorption coefficient, cm^{-1}
$\boldsymbol{\theta}$ = polar angle, rad
$\boldsymbol{\kappa}$ = effective volumetric absorption coefficient, cm^{-1}
$\boldsymbol{\xi}$ = distance traveled by a given photon, cm
$\boldsymbol{\rho}$ = density, g cm^{-3}; also reflectivity, dimensionless
$\boldsymbol{\phi}$ = azimuthal angle, rad
$\boldsymbol{\Omega}$ = solid angle, sr
$\boldsymbol{\Omega}$ = unit vector in the direction of propagation of a beam, dimensionless

Subscripts

di = relative to the direction of a given photon
loc = relative to the local value
max = relative to the maximum value
min = relative to the minimum value
ph = relative to a given photon
R = relative to the reflected radiation
S = relative to the surface
T = relative to the transmitted radiation
TiO_2 = relative to the TiO_2 films
V = relative to the volume
λ = denotes wavelength

Superscripts

$*$ = relative to the previous value in an iterative process
i = refers to the radiation incident on a given surface
t = refers to the radiation transmitted through a given surface

Special symbols

$\langle \cdot \rangle$ = means average value over a given interval
$\times$ = denotes cross product
$\bullet$ = denotes dot product

Literature Cited

1. Al-Ekabi H, Serpone N. Kinetic studies in heterogeneous photocatalysis. I. Photocatalytic degradation of chlorinated phenols in aerated aqueous solutions over TiO_2 supported on a glass matrix *J Phys Chem*. 1988;92:5726–5731.
2. Sclafani A, Brucato A, Rizzuti L. Mass transfer limitation in a packed bed photoreactor used for phenol removal. In: Ollis DF, Al-Ekabi H, editors. *Photocatalytic Purification and Treatment of Water and Air*. Amsterdam: Elsevier, 1993:533–545.
3. Crittenden JC, Suri RPS, Perram DL, Hand DW. Decontamination of water using adsorption and photocatalysis. *Water Res*. 1997;31:411–418.
4. Wang W, Chiang LW, Ku Y. Decomposition of benzene in air streams by UV/TiO_2 process. *J Hazard Mater*. 2003;101:133–146.
5. Zou L, Luo Y, Hooper M, Hu E. Removal of VOCs by photocatalysis process using adsorption enhanced TiO_2-SiO_2 catalyst. *Chem Eng Process*. 2006;45:959–964.
6. Ibhadon AO, Arabatzis IM, Falaras P, Tsoukleris D. The design and photoreaction kinetic modeling of a gas-phase titania foam packed bed reactor. *Chem Eng J*. 2007;133:317–323.
7. Changrani RG, Raupp GB. Monte Carlo simulation of the radiation field in a reticulated foam photocatalytic reactor. *AIChE J*. 1999;45:1085–1094.
8. Changrani RG, Raupp GB. Two-dimensional heterogeneous model for a reticulated-foam photocatalytic reactor. *AIChE J*. 2000;46:829–842.
9. Vorontsov AV, Savinov EE, Smirniotis PG. Vibrofluidized- and fixed-bed photocatalytic reactors: case of gaseous acetone photooxidation. *Chem Eng Sci*. 2000;55:5089–5098.

10. Alexiadis A, Baldi G, Mazzarino I. Modelling of a photocatalytic reactor with a fixed bed of supported catalyst. *Catal Today*. 2001;66: 467–474.
11. Loddo V, Imoberdorf GE, Augugliaro V, Yurdakal S, Irazoqui HA, Berber H, Palmisano G, Alfano OM, Palmisano L. Selective photocatalytic oxidation of 4-methoxybenzyl alcohol to *p*-anisaldehyde in organic-free water in a continuous annular fixed bed reactor. *Int J Chem Reactor Eng*. 2007;5:A57.
12. Spadoni G, Bandini E, Santarelli F. Scattering effects in photosensitized reactions. *Chem Eng Sci*. 1978;33:517–524.
13. Yokota T, Takahata Y, Nanjo H, Takahashi K. Estimation of light intensity in a solid-liquid photoreaction system. *J Chem Eng Jpn*. 1989;22:537–542.
14. Pasquali M, Santarelli F, Porter JF, Yue PL. Radiative transfer in photocatalytic systems. *AIChE J*. 1996;42:532–536.
15. Yokota T, Cesur S, Suzuki H, Baba H, Takahata Y. Anisotropic scattering model for estimation of light absorption rates in photoreactor with heterogeneous medium. *J Chem Eng Jpn*. 1999;32:314–321.
16. Yang Q, Ling Ang P, Ray MB, Pehkonen SO. Light distribution field in catalyst suspensions within an annular photoreactor. *Chem Eng Sci*. 2005;60:5255–5268.
17. Imoberdorf GE, Alfano OM, Cassano AE, Irazoqui HA. Monte Carlo model of UV-radiation interaction with TiO_2-coated spheres. *AIChE J*. 2007;53:2688–2703.
18. Brucato A, Cassano AE, Grisafi F, Montante G, Rizzuti L, Vella G. Estimating radiant fields in flat heterogeneous photoreactors by the Six-Flux model. *AIChE J*. 2006;52:3882–3890.
19. Brucato A, Grisafi F, Rizzuti L, Sclafani A, Vella G. Quasi-isoactinic reactor for photocatalytic kinetics studies. *Ind Eng Chem Res*. 2007;46:7684–7690.
20. Alexiadis A. 2-D radiation field in photocatalytic channels of square, rectangular, equilateral triangular and isosceles triangular sections. *Chem Eng Sci*. 2006;61:516–525.
21. Singh M, Salvado'-Estivill I, Li Puma G. Radiation field optimization in photocatalytic monolith reactors for air treatment. *AIChE J*. 2007;53:678–686.
22. Cassano AE, Martín CA, Brandi RJ, Alfano OM. Photoreactor analysis and design: fundamentals and applications. *Ind Eng Chem Res*. 1995;34:2155–2201.
23. Satuf ML, Brandi RJ, Cassano AE, Alfano OM. Experimental method to evaluate the optical properties of aqueous titanium dioxide suspensions. *Ind Eng Chem Res*. 2005;44:6643–6649.
24. Jacob SM, Dranoff JS. Light intensity profiles in a perfectly mixed photoreactor. *AIChE J*. 1970;16:359–363.
25. Blatchley ER III. Numerical modelling of UV intensity: application to collimated-beam reactors and continuous-flow systems. *Water Res*. 1997;31:2205–2218.
26. Akehata T, Shirai T. Effect of light-source characteristics on the performance of circular annular photochemical reactor. *J Chem Eng Jpn*. 1972;5:385–391.
27. Yokota T, Suzuki S. Estimation of light absorption rate in a tank type photoreactor with multiple lamps inside. *J Chem Eng Jpn*. 1995;28:300–305.
28. Irazoqui HA, Cerdá J, Cassano AE. Radiation profiles in an empty annular photoreactor with a source of finite spatial dimensions. *AIChE J*. 1973;19:460–467.
29. Stramigioli C, Santarelli F, Foraboschi FP. Photosensitized reactions in an annular continuous photoreactor. *Appl Sci Res*. 1977;33:23–44.
30. Siegel R, Howell JR. *Thermal Radiation Heat Transfer*, 4th ed. Bristol, PA: Hemisphere Publishing Corp., 2002.
31. Sodergren S, Hagfeldt A, Olsson J, Lindquist SE. Theoretical models for the action spectrum and the current-voltage characteristics of microporous semiconductor films in photoelectrochemical cells. *J Phys Chem*. 1994;98:5552–5556.

Appendix A

The reactor filling is considered as a population of a finite number of fibers. Each fiber is considered as a cylinder with a given radius ($R_{\text{fiber},i}$) and a given length ($L_{\text{fiber},i}$). To estimate the mean free path of the photons in the bed, the total sum of the fibers projected area is calculated:

$$A^{\text{long}}_{\text{fiber,T}} = \sum_{i=1}^{n_T} A^{\text{long}}_{\text{fiber,i}}, \tag{A1}$$

where $A^{\text{long}}_{\text{fiber},i}$ is the projected area of the ith quartz fiber, and n_T is the total number of fibers that comprises the reactor filling. Equation A1 can be expressed as follows:

$$A^{\text{long}}_{\text{fiber,T}} = \sum_{i=1}^{n_T} 2\, L_{\text{fiber,i}}\, R_{\text{fiber,i}}, \tag{A2}$$

where $L_{\text{fiber},i}$ and $R_{\text{fiber},i}$ is the length and radius of the ith quartz fiber, respectively. Then, the population of fibers can be expressed in terms of the number of fibers with a given radius (this consideration implies that the radius is assumed as a discrete variable):

$$A^{\text{long}}_{\text{fiber,T}} = \sum_{R=R_{\min}}^{R\max} 2\, R_{\text{fiber}} \sum_{j=1}^{n_R} L_{\text{fiber,R},j}. \tag{A3}$$

The sum of the lengths of the fibers with a given radius can be related with the mass of fibers with such radius as follows:

$$\mathrm{A}^{\text{long}}_{\text{fiber,T}} = \sum_{\mathrm{R=R\,min}}^{\mathrm{R\,max}} 2\, \mathrm{R}_{\text{fiber}} \frac{\mathrm{M_R}}{\rho_{\text{quartz}}\, \pi\, \mathrm{R}^2_{\text{fiber}}} = \frac{2}{\rho_{\text{quartz}}\, \pi} \sum_{\mathrm{R=R\,min}}^{\mathrm{R\,max}} \frac{\mathrm{M_R}}{\mathrm{R}_{\text{fiber}}}. \tag{A4}$$

After multiplying and dividing the right hand side of Eq. A4 by the mass of quartz fibers (M_{fiber}), and defining the mass percentage of a particular fiber radius as the mass of fibers with a given radius divided by the total mass of fibers, we obtain:

$$A^{\text{long}}_{\text{fiber,T}} = \frac{2\, M_{\text{fiber}}}{\rho_{\text{quartz}}\, \pi} \sum_{R=R_{\min}}^{R_{\max}} \frac{w_R}{R_{\text{fiber}}}, \tag{A5}$$

where the mass percentage of fibers with a given radius is

$$w_R = \frac{M_R}{M_{\text{fiber}}} = \frac{\sum_{j=1}^{n_R} \rho_{\text{quartz}}\, \pi\, R^2_{\text{fiber}}\, L_{\text{fiber,R},j}}{\sum_{R=R_{\min}}^{R_{\max}} \sum_{j=1}^{n_R} \rho_{\text{quartz}}\, \pi\, R^2_{\text{fiber}}\, L_{\text{fiber,R},j}}. \tag{A6}$$

Assuming that the mean length of the fibers ($\langle L_{\text{fiber}} \rangle$) is independent of their radius,

$$w_R = \frac{\langle L_{\text{fiber}} \rangle \sum_{j=1}^{n_R} R^2_{\text{fiber}}}{\langle L_{\text{fiber}} \rangle \sum_{R=R_{\min}}^{R_{\max}} \sum_{j=1}^{n_R} R^2_{\text{fiber}}} = \frac{n_R\, R^2_{\text{fiber}}}{\sum_{R=R_{\min}}^{R_{\max}} n_R\, R^2_{\text{fiber}}}. \tag{A7}$$

Replacing Eq. A7 in Eq. A5, we obtain:

$$A^{\text{long}}_{\text{fiber,T}} = \frac{2\,M_{\text{fiber}}}{\rho_{\text{quartz}}\,\pi}\sum_{R=R_{\min}}^{R_{\max}}\frac{1}{R_{\text{fiber}}}\frac{n_{\text{R}}\,R^2_{\text{fiber}}}{\sum_{R=R_{\min}}^{R_{\max}} n_{\text{R}}\,R^2_{\text{fiber}}}. \quad \text{(A8)}$$

Reorganizing Eq. A8, we arrive to the following equation:

$$A^{\text{long}}_{\text{fiber,T}} = \frac{2\,M_{\text{fiber}}}{\rho_{\text{quartz}}\,\pi}\frac{\sum_{R=R_{\min}}^{R_{\max}} n_{\text{R}}\,R_{\text{fiber}}}{\sum_{R=R_{\min}}^{R_{\max}} n_{\text{R}}\,R^2_{\text{fiber}}} \quad \text{(A9)}$$

where the sums indicated in the numerator and denominator of the right hand side of Eq. A9 are the first and second moments of the distributions of fiber radii, respectively, information that can be obtained from Figure 4b.

Appendix B

The thickness of the TiO_2 film can be calculated as follows:

$$t_{\text{k.TiO}_2} = \frac{M_{\text{TiO}_2}}{\rho_{\text{TiO}_2} A^{\text{ext}}_{\text{fiber,T}}}, \quad \text{(B1)}$$

where $A^{\text{ext}}_{\text{fiber,T}}$ is the sum of the external area of all the fibers:

$$A^{\text{ext}}_{\text{fiber,T}} = \sum_{i=1}^{n_T} 2\,\pi\,L_{\text{fiber,i}}\,R_{\text{fiber,i}}. \quad \text{(B2)}$$

Again, the population of fibers can be expressed in terms of the number of fiber of a given radius:

$$A^{\text{ext}}_{\text{fiber,T}} = \sum_{R=R_{\min}}^{R_{\max}} 2\,\pi\,R_{\text{fiber}}\sum_{j=1}^{n_{\text{R}}} L_{\text{fiber,R},j}, \quad \text{(B3)}$$

and relating the sum of the length of fibers whose radius is R with the mass of fibers with such radius:

$$A^{\text{ext}}_{\text{fiber,T}} = \sum_{R=R_{\min}}^{R_{\max}} 2\,\pi\,R_{\text{fiber}}\frac{M_{\text{R}}}{\rho_{\text{quartz}}\,\pi\,R^2_{\text{fiber}}} \quad \text{(B4)}$$

After multiplying the right hand term of Eq. B4 by the mass of quartz fibers:

$$A^{\text{ext}}_{\text{fiber,T}} = 2\,\pi\,M_{\text{fiber}}\sum_{R=R_{\min}}^{R_{\max}}\frac{w_{\text{R}}}{\rho_{\text{quartz}}\,\pi\,R_{\text{fiber}}} \quad \text{(B5)}$$

Substituting Eq. A7 into Eq. B5, we obtain:

$$A^{\text{ext}}_{\text{fiber,T}} = \frac{2\,M_{\text{fiber}}}{\rho_{\text{quartz}}}\frac{\sum_{R=R_{\min}}^{R_{\max}} n_{\text{R}}\,R_{\text{fiber}}}{\sum_{R=R_{\min}}^{R_{\max}} n_{\text{R}}\,R^2_{\text{fiber}}} \quad \text{(B6)}$$

Finally, replacing Eq. B6 into Eq. B1, we obtain:

$$t_{\text{k,TiO}_2} = \frac{M_{\text{TiO}_2}\,\rho_{\text{quartz}}}{2\,M_{\text{fiber}}\,\rho_{\text{TiO}_2}}\frac{\sum_{R=R_{\min}}^{R_{\max}} n_{\text{R}}\,R^2_{\text{fiber}}}{\sum_{R=R_{\min}}^{R_{\max}} n_{\text{R}}\,R_{\text{fiber}}} \quad \text{(B7)}$$

where the sums indicated in the numerator and denominator of the right hand side of Eq. B7 are the second and first moments of the distributions of fiber radii, respectively.

Manuscript received July 4, 2008, and revision received Jan. 20, 2009.